

Weakly Supervised Pneumonia Localization from Chest X-Rays Using Deep Neural Network and Grad-CAM Explanations

Kiran Shahi ^{1,*} and Anup Bagale ²

¹MBS Survey Software LTD., Steyning, United Kingdom

²Frontline Hospital, Kathmandu, Nepal

*Corresponding author(s). E-mail(s): ks@mbs-survey.co.uk;

Contributing authors: bagaleanup1@gmail.com;

August 2025

Abstract

This study proposes a weakly supervised deep learning framework for pneumonia classification and localization from chest X-rays, utilizing Grad-CAM explanations. Instead of costly pixel-level annotations, our approach utilizes image-level labels to generate clinically meaningful heatmaps that highlight regions affected by pneumonia. We evaluate seven ImageNet-pretrained architectures ResNet-18/50, DenseNet-121, EfficientNet-B0, MobileNet-V2/V3, and ViT-B16 under identical training conditions with focal loss and patient-wise splits to prevent data leakage. Experimental results on the Kermany CXR dataset demonstrate that ResNet-18 and EfficientNet-B0 achieve the best overall test accuracy of 98%, ROC-AUC = 0.997, and F1 = 0.987, while MobileNet-V2 provides an optimal trade-off between accuracy and computational cost. Grad-CAM visualizations confirm that the proposed models focus on clinically relevant lung regions, supporting the use of interpretable AI for radiological diagnostics. This work highlights the potential of weakly supervised explainable models that enhance pneumonia screening transparency, and clinical trust in AI-assisted medical imaging.

Keywords pneumonia localization, chest X-ray, weak supervision, Grad-CAM, explainable AI

1 Introduction

Pneumonia is still a leading cause of morbidity and mortality worldwide, especially among children and elderly individuals. Although chest X-ray imaging is

the most common diagnostic tool [1], interpreting chest X-rays can be a challenging task due to easily missed, subtle, and ambiguous lesions. Variability in radiologists’ interpretations and the frequent oversight of small abnormalities can make consistent diagnosis difficult [2]. These limitations highlight the need for reliable solutions. As artificial intelligence systems continue to mature, deep learning-based methods offer strong potential for the accurate and efficient detection of pneumonia.

Convolutional neural networks (CNNs) have demonstrated state of the art performance in various medical image analysis tasks, including pneumonia detection from chest X-rays[3]. However, most solutions operate as ”black-box” classifiers, offering limited insight into the image regions that drive their decisions. Since radiologists require transparent, localized explanations to verify model outputs, this lack of interpretability restricts clinical adoption. Moreover, pixel-level annotations, such as segmentation masks or bounding boxes, are necessary for fully supervised localization techniques; however, they are costly and challenging to acquire at scale [4].

Weakly supervised learning (WSL) techniques offer a practical approach for spatial localization using only image level labels, thereby avoiding the burdens of manual pixel wise annotations. Among various WSL approaches, Gradient-weighted Class Activation Mapping (Grad-CAM) has been widely adopted for visual explanations in radiology, highlighting the most influential regions that contribute to model predictions. Therefore, interpretable heatmaps generated using Grad-CAM enhance interpretability and provide clinicians with intuitive visual cues linking predictions to underlying radiographic features.

This study presents a unified framework for pneumonia classification and Grad-CAM based weakly supervised localization of pneumonia using chest X-rays. We benchmark seven different pre-trained model, such as ResNet-18[5], ResNet50[5], DenseNet121[6], EfficientNet-B0[7], MobileNetV2[8], MobileNetV3[9], and the transformer-based ViT-B16[10], under identical training conditions. We can compare performance across various design philosophies thanks to these models, which strike a balance between transformer-based, deep, and lightweight paradigms. We used publicly accessible CXR datasets to validate our approach, showing that it produces interpretable localizations aligned with radiological assessments and achieves high classification accuracy. This article highlights the potential of explainable and weakly supervised AI methods to narrow the gap between automated image interpretation and practical clinical decision-making. The main contributions of this paper are as follows:

- We evaluate Chest X-Rays dataset [3] with strict patient level split to prevent the data leakage.
- We benchmarked six pretrained CNN and Vision Transformer backbones under identical training and evaluation settings.
- We integrated Grad-CAM and token activation visualization to produce radiologically meaningful heatmaps aligned with lung regions, offering interpretable AI insights for clinicians.

- We identified MobileNet-V2 as an optimal trade off between accuracy and computational cost, supporting realtime, edge and mobile health application.

The remainder of the paper is organised as follows. Section 2 reviews previous studies on pneumonia detection, the class imbalance problem, and the use of explainability in pneumonia localisation. Section 3 describes the methods and neural architectures employed in the experiments. Section 4 presents the experimental setup, datasets, and analysis of the results. Finally, Section 5 provides the discussion and conclusion.

2 Related Work

Pneumonia is an enormous burden on societies in terms of healthcare costs, loss of young lives, and long-term consequences for families and communities. Alarmingly, a child dies from pneumonia every 43 seconds worldwide. It has a devastating impact and urgently needs effective early diagnosis and accessible treatment strategies [11]. Chest radiographs are traditionally used to diagnose pneumonia. The diagnosis is done manually, which comes with its own challenges. The manual diagnosis process is time-consuming, has greater variability, and is subjective.

With recent advancements in deep learning, AI-assisted medical imaging has achieved state of the art performance. Wang et al. developed the ChestX-ray14 dataset with over 112,000 images across 14 diseases, though only 1,500 images were labeled as pneumonia, creating a major class imbalance. They tested multiple deep learning architectures, including AlexNet, GoogleNet, ResNet, and VGG16, for abnormality classification. Among these, ResNet achieved the highest accuracy, demonstrating its superior performance for chest X-ray image analysis [12].

Ayan et al. compared two Convolution Neural Network architectures (VGG16 AND Xception). VGG16 achieved higher accuracy the Xception architecture. The accuracy of VGG16 was found to be 84.5 which shows the misclassification made by the model [13].

Benjamin Antin et al. applied a supervised learning approach on the ChestX-ray14 dataset for binary classification of pneumonia versus non-pneumonia. Due to resource limitations, they analyzed 5,606 random images using k-means clustering and logistic regression with the Adam optimizer. Their findings showed that logistic regression struggled with the dataset’s complexity, while a DenseNet model achieved better performance with an AUC of 0.60 [14].

Shahida et al. used chest X-ray data from multiple public sources (IEEE, Mendel, Kaggle, NIH) containing classes such as normal, pneumonia, COVID-19, and other lung diseases to detect and classify pneumonia. Logistic Regression, Naïve Bayes, k-Nearest Neighbors (kNN), Decision Tree, Random Forest, Support Vector Machine (SVM), Ridge Regression, and LASSO were applied. On unsegmented balanced data, SVM achieved the highest testing accuracy

(74.66). The performance dropped significantly in unbalanced settings, especially in terms of test accuracy and balanced accuracy [15].

Hasmi et al. proposed a pneumonia detection model for chest X-ray images using transfer learning with multiple state-of-the-art CNNs (ResNet18, Xception, InceptionV3, DenseNet121, MobileNetV3). Partial data augmentation was applied to balance the dataset, and a weighted classifier was built to optimally combine predictions from the individual models. Using multiple pre-trained models in an ensemble indicates that no single model was sufficient across all cases. The final weighted ensemble achieved 98.43 test accuracy and 99.76 AUC on unseen data [16].

Alireza Saber et al. introduced a multi-scale transformer-based framework along with lung segmentation to improve pneumonia detection from chest X-rays. They masked out non-lung regions and combined local and global features through attention and transformer modules. The model achieved higher accuracy and better generalization than standard CNN classifiers [17].

Krishna Nand Keshavamurthy et al. proposed a weakly supervised GAN-based framework to localize pneumonia in chest X-rays without requiring costly bounding-box annotations. This method generated pseudo-normal images and computed abnormality maps. It highlighted pneumonia regions more precisely than conventional classification models that rely on CAMs. The study demonstrated key limitations of supervised approaches, such as dependence on expensive expert annotations, coarse localization, and poor generalization [18].

Kairou Guo et al. developed a ResNet-34 based weakly supervised model trained on image-level labels to classify pneumonia in chest X-rays. By using CAMs, the model achieved a coarse localization of pneumonia regions without requiring detailed annotations. The results showed very high performance, with an AUC of 0.9949 on the internal test set and 0.9835 on external multi-center data, including COVID-19 cases [19].

Odiabo et al. introduced a weakly supervised ResNet-34 model trained solely on image-level labels in order to classify pneumonia in chest X-rays. The Utilization of Class Activation Maps (CAMs), helped model to achieve coarse localization of pneumonia regions without requiring detailed annotations. Performance metrics include an AUC of 0.9949, accuracy of 98.29, sensitivity of 99.29, and specificity of 95.87 on an internal test set [20].

3 Methods

Our approach follows a standard deep learning pipeline consisting of dataset preprocessing, backbone model selection, training and evaluation of model performance. We designed the method to emphasize weakly supervised localization while ensuring reproducibility and robustness across multiple architectures.

3.1 Dataset

We used the publicly available Chest X-ray dataset [3]. In this dataset, 1583 X-ray images are in normal class and 4273 are in pneumonia class including both train and test set. In train set 1349 images are in normal class and 3884 images are in pneumonia class. Similarly, in train set 234 images are in normal class and 390 images are in pneumonia class. However, while exploring the dataset we found that some patients id were on both test and train set which could cause data leakage. To avoid this we merged both train and test and group by patient id and re-spilted to train, validation and test set containing 70, 15 and 15 percentage of data respectively. Each image was resize to 224 x 224 pixels to match the input requirements of ImageNet-pretrained backbones. Since the original images were grayscale, we duplicated the channel three times to create a pseudo-RGB input to match the input shape for pretrained backbones. Further, to enhance generalization, we applied data augmentation including random rotation, horizontal flipping, brightness/contrast adjustment, and Gaussian noise. Dataset splitting was performed at the patient level to prevent data leakage, with 70% of patients for training, 15% for validation, and 15% for testing.

Table 1: Patient-level dataset distribution after re-splitting.

Subset	NORMAL	PNEUMONIA
Train (70%)	1,114	2,951
Validation (15%)	232	653
Test (15%)	237	669

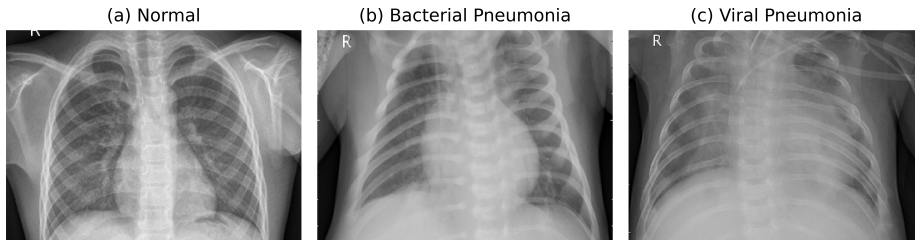


Figure 1: Sample chest X-ray images from the dataset: (a) Normal, (b) Pneumonia (Bacterial), and (c) Pneumonia (Viral).

3.2 Model Architectures

We evaluated a diverse set of ImageNet pretrained backbones to capture different trade-offs between accuracy, efficiency and representational power. These backbones represent residual networks, densely connected networks, parameter-efficient scaling methods, mobile-optimized networks, and transformer-based architectures.

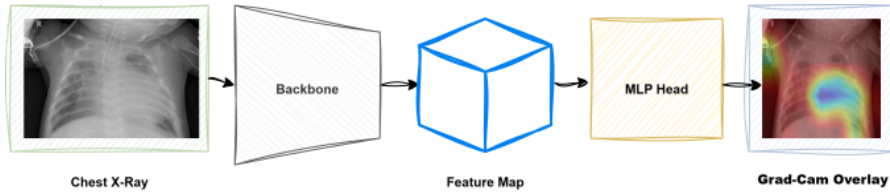


Figure 2: Model Architecture

- **ResNet18 and ResNet50:** Residual networks mitigate the vanishing gradient problem by introducing skip connections that allow gradients to flow across layers[5]. ResNet-18 provides a lightweight baseline, while ResNet-50, with its deeper architecture, captures more complex hierarchical features.
- **DenseNet121:** DenseNet improves feature reuse and gradient propagation by connecting each layer to all subsequent layers[6]. This design leads to compact models with fewer parameters while retaining strong representational capacity
- **EfficientNet-B0:** EfficientNet introduces a compound scaling method that uniformly scales depth, width and resolution using a fixed coefficient [7]. This results in highly parameter-efficient models that achieve strong accuracy with fewer computational resources.
- **MobileNetV2:** MobileNetV2 is designed for mobile and edge deployment, using inverted residuals with linear bottlenecks to reduce computational cost without sacrificing accuracy [8].
- **MobileNetV3:** An evolution of MobileNetV2, MobileNetV3 incorporates automated network architecture search and squeeze-and-excitation modules, providing an improved trade-off between latency and accuracy [9].
- **ViT-B16:** The Vision Transformer (ViT) replaces convolutional operations with self-attention mechanisms, dividing an image into non-overlapping patches and modeling global dependencies between them[10]. We included ViT-B16 to compare transformer-based architectures with traditional CNNs.

All backbones were integrated with a uniform custom classification head consisting of fully connected, batch normalization, ReLU activation and dropout layers ensuring fair comparison across architectures.

3.3 Training Procedure

All models were initialized with ImageNet-pretrained weights to leverage transfer learning. Training was conducted under identical protocols to ensure a fair

comparison between backbones.

- **Input preprocessing:** Each image was resized to 224×224 pixels and normalized with ImageNet mean and standard deviation. Since the dataset is grayscale, the channel was duplicated three times to create a pseudo-RGB input to match the input shape of pretrained models.
- **Data augmentation:** To improve generalization and mitigate overfitting, $\pm 15^\circ$ rotations, $\pm 5\%$ affine transformation, 5% brightness contrast adjustment, CLAHE, gamma correction, Gaussian noise, motion blur, median blur and coarse dropout were applied.
- **Loss functions:** We evaluated three options Cross-Entropy Loss, Weighted Cross-Entropy Loss, and Focal Loss [21]. Focal Loss was ultimately chosen as it provided improved handling of the severe class imbalance (404 normal vs. 3692 pneumonia images).

The Focal Loss is an extension of the standard binary cross-entropy to better handle class imbalance by reducing the relative loss for well-classified class. It introduces a focusing parameter γ that down-weights easy samples, allowing the model to concentrate more on hard or misclassified cases. Mathematically the the binary focal loss function is defined as:

$$L(y, \hat{p}) = -\alpha y(1 - \hat{p})^\gamma \log(\hat{p}) - (1 - \alpha)(1 - y) \hat{p}^\gamma \log(1 - \hat{p})$$

where $y \in \{0, 1\}$ is the ground-truth label and $\hat{p} \in [0, 1]$ is the predicted probability for the positive class. The parameter γ controls how strongly easy examples are down weighted higher values increase the focus on hard samples while α balances the importance between positive and negative classes. When $\gamma = 0$, the Focal Loss simplifies to the standard weighted binary cross-entropy loss.

- **Class imbalance strategies:** In addition to Focal Loss, we applied random over-sampling of minority class during training. This ensured that each mini-batch was more balanced and prevented the model from being biased toward the pneumonia class.
- **Optimizer and hyperparameters:** Models were optimized with the Adam optimizer (learning rate = 1×10^{-4} , weight decay = 1×10^{-4}). The batch size was set to 32, and training was run for 10 epochs.
- **Model checkpointing and early stopping:** The best model checkpoint for each architecture was selected based on the highest validation accuracy and ROC-AUC. Early stopping was used to prevent overfitting when validation performance did not improve for several epochs.
- **Evaluation:** After training, each model was tested on an independent patient-level test set. Metrics included accuracy, ROC-AUC, PR-AUC and best F1-score across thresholds.

3.4 Performance Evaluation Metrics

To comprehensively assess model performance, we adopted evaluation metrics that capture both classification accuracy and clinical relevance under class-imbalanced settings.

Let TP, TN, FP, and FN denote true positives, true negatives, false positives, and false negatives, respectively.

Accuracy:

$$\text{Accuracy} = \frac{\text{TP} + \text{TN}}{\text{TP} + \text{TN} + \text{FP} + \text{FN}}$$

Precision (Positive Predictive Value):

$$\text{Precision} = \frac{\text{TP}}{\text{TP} + \text{FP}}$$

Recall (Sensitivity / True Positive Rate):

$$\text{Recall} = \frac{\text{TP}}{\text{TP} + \text{FN}}$$

Specificity (True Negative Rate):

$$\text{Specificity} = \frac{\text{TN}}{\text{TN} + \text{FP}}$$

F1-score:

$$F1 = 2 \cdot \frac{\text{Precision} \cdot \text{Recall}}{\text{Precision} + \text{Recall}}$$

The harmonic mean of precision and recall. We report the *Best F1-score* obtained across thresholds.

ROC-AUC (Receiver Operating Characteristic – Area Under the Curve): ROC curves plot sensitivity against $1 - \text{Specificity}$ across thresholds. The AUC summarizes overall discriminative ability independent of threshold.

PR-AUC (Precision–Recall – Area Under the Curve): PR curves plot precision against recall. The AUC provides insight into model performance under severe class imbalance, emphasizing minority class detection.

3.5 Pneumonia Localization

To highlight the most influential regions in predictions, we employ Gradient weighted Class Activation Mapping (Grad-CAM) [22] serving as a weakly supervised localization mechanism and enhancing clinical interpretability. For CNN based architectures, Grad-CAM is computed using the feature maps and gradients of the last convolution layer, which provide a direct spatial correspondence with the input image. Whereas, ViT operate on patch embeddings instead of convolution features, therefore we extend Grad-CAM formulation by capturing activations and gradients from the final MLP block of the last transformer encoder layer.

3.5.1 Grad-CAM for CNN Architectures

In convolutional architectures such as ResNet, DenseNet, and MobileNet, Grad-CAM is applied to the *last convolutional layer*, which retains the highest-level semantic and spatial information. Let $A \in \mathbb{R}^{C \times H \times W}$ denote the activation maps of this layer, and $\nabla Y_c \in \mathbb{R}^{C \times H \times W}$ represent the gradients of the predicted class score Y_c with respect to these activations. The channel-wise importance weights are obtained by global average pooling of the gradients:

$$\alpha_k = \frac{1}{HW} \sum_{i=1}^H \sum_{j=1}^W \nabla Y_c[k, i, j], \quad (1)$$

and the class-discriminative heatmap is computed as:

$$\text{CAM}(i, j) = \text{ReLU} \left(\sum_{k=1}^C \alpha_k A_k(i, j) \right). \quad (2)$$

The resulting activation map is upsampled to match the original image resolution and combined with the input image to generate a heatmap overlay that highlights the regions most responsible for the model’s decision.

3.5.2 Grad-CAM for Vision Transformers

Vision Transformers (ViTs) replace convolutional filters with tokenized patch embeddings, requiring a modification of the Grad-CAM formulation. We capture activations from the *final Linear layer of the last MLP block* within the last transformer encoder, which preserves spatially meaningful representations for all image patches. Let $A \in \mathbb{R}^{N \times C}$ be the activations of N patch tokens (excluding the class token) and $\nabla Y_c \in \mathbb{R}^{N \times C}$ the corresponding gradients of the predicted class. The importance weights are computed as:

$$\alpha_k = \frac{1}{N} \sum_{i=1}^N \nabla Y_c[i, k], \quad (3)$$

and the patch-level class activation map is obtained as:

$$\text{CAM}(i) = \text{ReLU} \left(\sum_{k=1}^C \alpha_k A[i, k] \right). \quad (4)$$

The one-dimensional patch map is reshaped into a 2D grid ($H_p \times W_p$) based on the number of patches and subsequently upsampled to the input image resolution. The resulting heatmap is overlaid on the original image to visualize the spatial contribution of each patch to the prediction.

This unified Grad-CAM framework provides consistent visual interpretability across both CNN and transformer-based backbones, enabling qualitative comparison of their attention on diagnostically relevant regions.

4 Experiments

The details of the experiments, including the datasets, loss functions, model training, results and analysis are described as follows:

4.1 Experimental Setup

All models were trained under identical conditions to ensure fair comparison. Training and evaluation were performed using PyTorch 2.8.0+cu126 on an NVIDIA T4 GPU with 15 GB VRAM. The batch size was 32, learning rate 1×10^{-4} , and weight decay 1×10^{-4} . Each model was trained for 10 epochs with early stopping based on validation ROC-AUC. The best checkpoint per backbone was saved and later evaluated on the independent test split. Evaluation metrics include Accuracy, ROC-AUC, PR-AUC and Best F1.

4.2 Result

Table 2: Performance comparison among the evaluated architectures on the Chest X-Rays dataset [3].

Model	Val Acc	Test Acc	ROC-AUC	PR-AUC	F1 score	Param (M)
ResNet-18	97.5%	98%	0.9971	0.9990	0.987	11.5
ResNet-50	96.8%	96%	0.9952	0.9983	0.981	24.6
DenseNet-121	97.9%	97%	0.9955	0.9984	0.984	7.5
EfficientNet-B0	96.9%	98%	0.9971	0.9989	0.987	4.7
MobileNet-V2	95.6%	97%	0.9946	0.9980	0.982	2.9
MobileNet-V3	96.2%	97%	0.9971	0.9990	0.987	4.9
ViT	96.2%	97%	0.9971	0.9990	0.987	86.2

Overall, all evaluated architectures achieved strong discriminative performance on the pneumonia classification task, with test accuracies ranging between 96–98%. Among them, **ResNet-18** and **EfficientNet-B0** achieved the highest test accuracy of 98% and an F1-score of 0.987, while maintaining ROC-AUC and PR-AUC values above 0.997. Despite its smaller size, **MobileNet-V3 Large** delivered comparable accuracy (97%), demonstrating its suitability for mobile and embedded clinical applications. Deeper backbones such as **ResNet-50** and **DenseNet-121** showed marginally lower generalization, suggesting mild overfitting to the training set. These findings indicate that compact architectures, when combined with focal loss and patient-wise splitting, can achieve state-of-the-art accuracy while remaining computationally efficient. Qualitative Grad-CAM visualizations (Figure 3) further confirm that the models correctly focus on radiologically relevant lung regions, reinforcing interpretability and clinical trust.

Figure 3 illustrates Grad-CAM overlays for representative samples of normal, bacterial, and viral pneumonia across the evaluated architectures. For normal

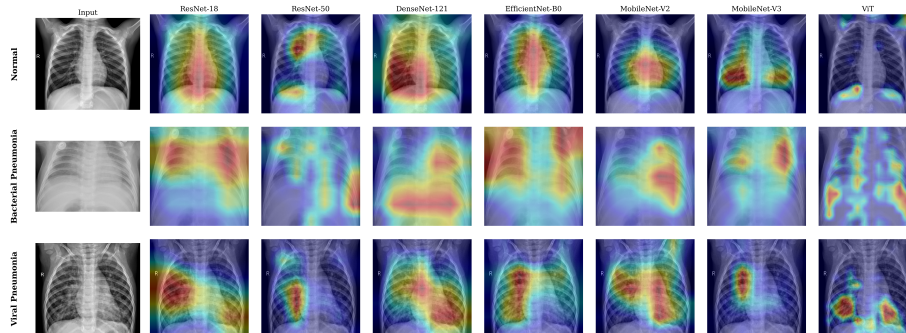


Figure 3: Grad-CAM overlays for a normal chest X-ray and two pneumonia cases (bacterial, viral) across seven backbones. Bright regions indicate strong model attention toward pneumonia related features.

x-ray, the activation responses were weak and dispersed outside the lung, indicating that models correctly assigned to low confidence to non pathological region. An Exception was DenseNet-121, which spurious activation along the left lung region, suggesting a mild over-sensitivity to background intensity variations or residual noise.

In contrast, pneumonia cases produced focused, high-intensity activations within the pulmonary zones corresponding to radiographic opacities particularly in the lower and middle lobes.

Among the evaluated backbones, MobileNet-V2 produced the most compact and noise free localization across all categories (i.e. Normal, Bacterial and Viral pneumonia), while ResNet-18 and DenseNet-121 showed equally strong and well defined activations for pneumonia class. Although EfficientNet-B0 achieved high classification accuracy, its Grad-CAM visualizations were less spatially aligned with radiological abnormalities, showing diffuse or midline-biased response. Similarly, ResNet-50 also displayed occasional off-target hotspots. The ViT-B16 model highlighted broader lung areas due to its global self-attention, capturing contextual cues but with reduced localization sharpness.

Overall, the Grad-CAM overlays demonstrate that the proposed models predominantly attend to clinically meaningful lung regions, most convincingly MobileNet-V2, reinforcing the interpretability and potential for trustworthy AI assisted pneumonia screening.

5 Conclusion and Future Works

This study benchmarked multiple CNN backbones and Vision Transformer for weakly supervised pneumonia localization using only image level supervision. All models achieved high discriminative performance, with test accuracies ranging from 96% to 98%. ResNet-18 and EfficientNet-B0 consistently outperformed deeper networks, demonstrating that compact architectures can generalize well

when trained with class-balanced sampling and focal loss. Grad-CAM heatmaps confirmed that attention focused on radiologically relevant opacities, validating interpretability and trustworthiness. The results further show that lightweight models, such as MobileNet-V2, can deliver near state of the art (SOTA) accuracy with low computational cost, facilitating edge device or mobile health deployments.

Although the proposed framework demonstrates the effectiveness of Grad-CAM based weakly supervised localization for pneumonia detection, several opportunities for extension remain open for future investigations, as outlined below.

- This research is currently limited to a single dataset. Further work should involve evaluation on larger and more diverse datasets, such as RSNA Pneumonia and NIH ChestX-ray14, to enhance robustness and generalization.
- Due to the absence of lesion level annotations on the dataset, this research lacks the quantitative evaluation of Grad-CAM based localization. In future studies, bounding box based metrics such as IoU can be incorporated to evaluate the localization performance once annotated datasets are available.
- Further extensions may explore multi-label thoracic disease localization, radiologist reader studies, and mobile deployment optimizations to strengthen the framework’s clinical relevance and translational impact.

Overall, this study highlights that explainable and weakly supervised deep-learning methods can bridge the gap between black-box image classification and clinically interpretable decision support for pneumonia detection.

Author Contributions

K.S.: conceptualization, methodology, software; K.S. and A.B.: data curation, writing—original draft preparation; K.S. and A.B.: visualization, investigation; K.S.: supervision; K.S. and A.B.: software, validation; writing—reviewing and editing. All authors have read and agreed to the published version of the manuscript.

Funding

This research received no external funding

Institutional Review Board Statement

Not applicable

Informed Consent Statement

Not applicable

Data Availability Statement

The dataset used in this study is publicly available (see Reference [3] for the Kermany dataset). The source code supporting the findings of this study is available at: <https://github.com/kiranshahi/pneumonia-analysis>.

Acknowledgments

The author acknowledges the use of the Chest X-ray dataset by Kermany et al. [3].

Conflict of Interest Disclosure

The author declares no conflict of interest.

References

- [1] Angela Bartolf and Catherine Cosgrove. Pneumonia. *Medicine*, 44(6):373–377, 2016. Respiratory Disorders (Part 3 of 3).
- [2] Alan Ropp, Stephen Waite, Deborah Reede, and Jay Patel. Did i miss that: Subtle and commonly missed findings on chest radiographs. *Current Problems in Diagnostic Radiology*, 44(3):277–289, 2015.
- [3] Daniel S. Kermany, Michael Goldbaum, Wenjia Cai, Carolina C.S. Valentin, Huiying Liang, Sally L. Baxter, Alex McKeown, Ge Yang, Xiaokang Wu, Fangbing Yan, Justin Dong, Made K. Prasadha, Jacqueline Pei, Magdalene Y.L. Ting, Jie Zhu, Christina Li, Sierra Hewett, Jason Dong, Ian Ziyar, Alexander Shi, Runze Zhang, Lianghong Zheng, Rui Hou, William Shi, Xin Fu, Yaou Duan, Viet A.N. Huu, Cindy Wen, Edward D. Zhang, Charlotte L. Zhang, Oulan Li, Xiaobo Wang, Michael A. Singer, Xiaodong Sun, Jie Xu, Ali Tafreshi, M. Anthony Lewis, Huimin Xia, and Kang Zhang. Identifying medical diagnoses and treatable diseases by image-based deep learning. *Cell*, 172(5):1122–1131.e9, 2018.
- [4] Geert Litjens, Thijs Kooi, Babak Ehteshami Bejnordi, Arnaud Arindra Adiyoso Setio, Francesco Ciompi, Mohsen Ghafoorian, Jeroen A.W.M. van der Laak, Bram van Ginneken, and Clara I. Sánchez. A survey on deep learning in medical image analysis. *Medical Image Analysis*, 42:60–88, 2017.
- [5] Kaiming He, Xiangyu Zhang, Shaoqing Ren, and Jian Sun. Deep residual learning for image recognition. In *Proceedings of the IEEE Conference on Computer Vision and Pattern Recognition (CVPR)*, June 2016.
- [6] Gao Huang, Zhuang Liu, Laurens van der Maaten, and Kilian Q. Weinberger. Densely connected convolutional networks. In *Proceedings of the IEEE Conference on Computer Vision and Pattern Recognition (CVPR)*, July 2017.

- [7] Mingxing Tan and Quoc Le. EfficientNet: Rethinking model scaling for convolutional neural networks. In Kamalika Chaudhuri and Ruslan Salakhutdinov, editors, *Proceedings of the 36th International Conference on Machine Learning*, volume 97 of *Proceedings of Machine Learning Research*, pages 6105–6114. PMLR, 09–15 Jun 2019.
- [8] Mark Sandler, Andrew Howard, Menglong Zhu, Andrey Zhmoginov, and Liang-Chieh Chen. Mobilenetv2: Inverted residuals and linear bottlenecks. In *Proceedings of the IEEE Conference on Computer Vision and Pattern Recognition (CVPR)*, June 2018.
- [9] Andrew Howard, Mark Sandler, Grace Chu, Liang-Chieh Chen, Bo Chen, Mingxing Tan, Weijun Wang, Yukun Zhu, Ruoming Pang, Vijay Vasudevan, Quoc V. Le, and Hartwig Adam. Searching for mobilenetv3. In *Proceedings of the IEEE/CVF International Conference on Computer Vision (ICCV)*, October 2019.
- [10] Alexey Dosovitskiy, Lucas Beyer, Alexander Kolesnikov, Dirk Weissenborn, Xiaohua Zhai, Thomas Unterthiner, Mostafa Dehghani, Matthias Minderer, Georg Heigold, Sylvain Gelly, Jakob Uszkoreit, and Neil Houlsby. An image is worth 16x16 words: Transformers for image recognition at scale. *arXiv preprint arXiv:2010.11929*, 2020.
- [11] Ignacio Castro-Aguirre, Dan Alvarez, Marcela Contreras, Pierce Trumbo, Oscar Mujica, Daniel Peraza, and Martha Patricia Velandia-Gonzalez. The impact of the coronavirus pandemic on vaccination coverage in latin america and the caribbean. *Vaccines*, 12:458, 04 2024.
- [12] Ritika Nandi and Manjunath Mulimani. Detection of covid-19 from x-rays using hybrid deep learning models. *Research on Biomedical Engineering*, 37(4):687–695, 2021.
- [13] Enes Ayan and Halil Murat Ünver. Diagnosis of pneumonia from chest x-ray images using deep learning. In *2019 Scientific Meeting on Electrical-Electronics & Biomedical Engineering and Computer Science (EBBT)*, pages 1–5, 2019.
- [14] Nada M Elshennawy and Dina M Ibrahim. Deep-pneumonia framework using deep learning models based on chest x-ray images. *Diagnostics*, 10(9):649, 2020.
- [15] Shahida Parveen and Khan Bahadar Khan. Detection and classification of pneumonia in chest x-ray images by supervised learning. In *2020 IEEE 23rd International Multitopic Conference (INMIC)*, pages 1–5, 2020.
- [16] Mohammad Farukh Hashmi, Satyarth Katiyar, Avinash G Keskar, Neeraj Dhanraj Bokde, and Zong Woo Geem. Efficient pneumonia detection in chest xray images using deep transfer learning. *Diagnostics*, 10(6):417, 2020.

- [17] Alireza Saber, Pouria Parhami, Alimohammad Siahkarzadeh, Mansoor Fateh, and Amirreza Fateh. Efficient and accurate pneumonia detection using a novel multi-scale transformer approach. *arXiv preprint arXiv:2408.04290*, 2024.
- [18] Krishna Nand Keshavamurthy, Carsten Eickhoff, and Krishna Juluru. Weakly supervised pneumonia localization in chest x-rays using generative adversarial networks. *Medical physics*, 48(11):7154–7171, 2021.
- [19] Kairou Guo, Jiangbo Cheng, Kaiyuan Li, Lanhui Wang, Yadong Lv, and Desen Cao. Diagnosis and detection of pneumonia using weak-label based on x-ray images: a multi-center study. *BMC Medical Imaging*, 23(1):209, 2023.
- [20] David Odaibo, Zheng Zhang, Frank Skidmore, and Murat Tanik. Detection of visual signals for pneumonia in chest radiographs using weak supervision. In *2019 SoutheastCon*, pages 1–5. IEEE, 2019.
- [21] Tsung-Yi Lin, Priya Goyal, Ross Girshick, Kaiming He, and Piotr Dollár. Focal loss for dense object detection. *IEEE Transactions on Pattern Analysis and Machine Intelligence*, 42(2):318–327, 2020.
- [22] Ramprasaath R. Selvaraju, Michael Cogswell, Abhishek Das, Ramakrishna Vedantam, Devi Parikh, and Dhruv Batra. Grad-CAM: Visual Explanations from Deep Networks via Gradient-Based Localization . In *2017 IEEE International Conference on Computer Vision (ICCV)*, pages 618–626, Los Alamitos, CA, USA, October 2017. IEEE Computer Society.